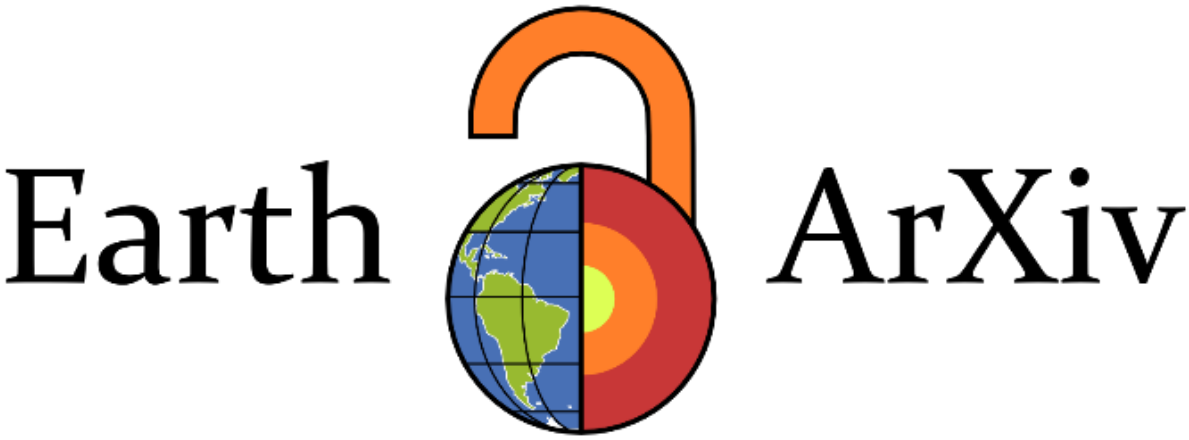

A machine learning-based vanadium-in-magnetite-clinopyroxene oxybarometer for constraining oxygen fugacity in mafic–ultramafic intrusions

Guang-Shao Wang[1,2], Zhong-Jie Bai[1*], Jian-Feng Gao[1], Wen-Jun Hu[1], Jun-hua Yao[1], Wei-Guang Zhu[1]

[1] State Key Laboratory of Critical Mineral Research and Exploration, Institute of Geochemistry, Chinese Academy of Sciences, Guiyang 550081, China

[2] University of Chinese Academy of Sciences, Beijing 100049, China

* Corresponding author: Zhong-Jie Bai (baizhongjie@vip.gyig.ac.cn)

Abstract

Reliable reconstruction of primary magmatic oxygen fugacity (fO_2) in plutonic systems remains challenging because existing oxybarometers either require equilibrium melt compositions or preferentially record late-stage oxide equilibration, limiting their ability to constrain primary magmatic redox conditions. Here we develop a machine-learning framework that transfers experimentally calibrated V partitioning between clinopyroxene (Cpx)–melt and magnetite (Mt)–melt to a melt-independent Mt–Cpx oxybarometer. The framework also yields complementary V-in-Cpx and V-in-Mt oxybarometers for systems in which equilibrium melts are available or can be independently reconstructed. The calibrated models accurately reproduce experimental V partitioning and fO_2 over a wide range of temperatures, fO_2, and compositions. Model interpretation indicates that V partitioning provides the primary control on predicted fO_2, whereas temperature and mineral–melt chemistry mainly account for equilibrium-related corrections. Comparisons with independently constrained experimental fO_2 and established mineral-based oxybarometers demonstrate robust predictive performance and broad applicability to natural magmatic systems. Application of the melt-independent V-in-Mt–Cpx oxybarometer to the Panzhihua intrusion and the Upper Zone of the Bushveld Complex reveals contrasting redox evolution during magma differentiation. Panzhihua preserves persistently oxidized conditions (ΔFMQ= +1.29 to +1.99), consistent with redox buffering by repeated recharge of relatively oxidized magma, whereas the Bushveld Upper Zone records progressive reduction (ΔFMQ= +0.06 to +1.31) associated with differentiation in a predominantly closed magmatic system. These results demonstrate that mineral-pair V partitioning provides a practical means of reconstructing magmatic redox evolution in plutonic

rocks and offers new insights into the links among magma dynamics, oxygen fugacity, and Fe–Ti–V oxide

Keywords: V-in-magnetite–clinopyroxene oxybarometer; oxygen fugacity; machine learning; mafic-ultramafic intrusions; magma evolution

1. Introduction

Oxygen fugacity (fO_2) is a key thermodynamic parameter that controls the redox state of magmatic systems. It plays a fundamental role in regulating element valence and partitioning, mineral crystallization, sulfide saturation, and metal enrichment (Hirschmann et al. 2012, Namur et al. 2016, Armstrong et al. 2019, Gennaro et al. 2020, Alex and Zajacz 2022, Ge et al. 2023). Mafic–ultramafic intrusions, represented by the Bushveld Complex and the Panxi layered intrusions, are important host rocks for Fe–Ti–V oxide deposits and Cu–Ni–PGE sulfide deposits(Cawthorn 2010, Bai et al. 2012, 2019). Accurately constraining the fO_2 of these systems during the magmatic stage and its subsequent evolution is therefore critical for understanding magma differentiation and related ore formation mechanisms(Bai et al. 2012, Liao et al. 2016, Cao et al. 2020). However, due to methodological limitations, particularly those arising from prolonged cooling and post-magmatic modification that may disturb or reset primary mineral redox records, the reliable reconstruction of fO_2 in mafic–ultramafic intrusions remains a significant challenge (Holness et al. 2007, Leuthold et al. 2014, Charlier et al. 2015) ,.

Several mineral-based oxybarometers have been developed to quantify magmatic fO_2, but their application to layered intrusions remains limited. Recently developed Fe-, Ti-, and V-based magnetite–melt oxybarometers assume that magnetite crystallized in equilibrium with its parental melt(Arató and Audétat 2017*a*, *b*, Shepherd et al. 2022*a*) , and therefore require the

composition of the equilibrium melt. In plutonic rocks, however, such melts are rarely preserved and are difficult to reconstruct with confidence (Charlier et al. 2015, Dygert et al. 2025)), substantially restricting the application of mineral–melt oxybarometers. Magnetite–ilmenite oxybarometry avoids the need for melt compositions, but typically records the temperature and fO_2 of the final equilibration between the two oxides rather than primary magmatic conditions (Andersen et al. 1993, Ghiorso and Evans 2008) . Experimental studies demonstrate that Fe–Ti oxides readily re-equilibrate during subsolidus cooling(Hammond and Taylor 1982, Lattard et al. 2012, Hou et al. 2021) , whereas large layered intrusions may cool over timescales of 10^4–10^6 years(Zeh et al. 2015, Tavazzani et al. 2020, Grocolas et al. 2025) . Consequently, conventional oxide oxybarometers commonly record late-stage equilibration rather than the redox conditions prevailing during magma differentiation and ore formation(Loucks et al. 2018, Hou et al. 2021). Existing approaches therefore face a common limitation: they either require equilibrium melt compositions or record the fO_2 of late-stage oxide equilibration rather than primary magmatic conditions

Vanadium provides an attractive alternative because its valence state and partitioning behavior vary systematically with fO_2(Toplis and Corgne 2002, Mallmann and O'Neill 2009, 2013, Davis et al. 2013, Wang et al. 2019, Leuthold et al. 2023). Compared with major-element Fe–Ti exchange, V diffuses relatively slowly and is therefore less susceptible to subsolidus re-equilibration, allowing V partitioning to better preserve primary magmatic redox information (Mallmann and O'Neill 2013, Arató and Audétat 2017*a*, Sievwright et al. 2020). Although mineral–melt V partitioning has been successfully applied to estimate fO_2, its application to plutonic rocks remains hindered by the absence of equilibrium melts. Magnetite (Mt) and clinopyroxene (Cpx), in contrast, are widespread, commonly coexist throughout the

crystallization history of mafic magmas, and generally preserve primary major- and trace-element compositions. V partitioning between coexisting Mt and Cpx therefore has the potential to provide a fully mineral-based redox proxy that circumvents the need for melt reconstruction(Canil 1999, Mallmann and O'Neill 2009, Papike et al. 2013, Holycross and Cottrell 2022*a*, Shepherd et al. 2022*b*). However, experimental datasets containing paired V analyses for coexisting magnetite and clinopyroxene remain too limited to calibrate such a relationship directly. Recent advances in machine learning provide an effective means of extracting nonlinear relationships from experimental petrological datasets and therefore offer a promising approach for transferring experimentally calibrated mineral–melt partitioning relationships to mineral–mineral systems (Zou et al. 2024; Wang et al. 2025).

Here, we develop a machine-learning-based V partitioning oxybarometer for coexisting magnetite and clinopyroxene. To overcome the scarcity of paired Mt–Cpx experimental data, we first calibrate V partitioning between clinopyroxene and melt and between magnetite and melt using compiled experimental datasets. These experimentally constrained mineral–melt partitioning models are subsequently transferred to the directly measurable Mt–Cpx mineral pair, establishing a melt-independent V-in-Mt–Cpx oxybarometer. The same mineral–melt calibrations are also inverted to develop complementary V-in-Cpx and V-in-Mt oxybarometers for systems in which equilibrium melt compositions are available or can be independently constrained.

The proposed framework is evaluated through a series of partitioning, experimental, and natural sample tests. The mineral–melt partitioning models are first validated by comparing predicted and measured experimental V partition coefficients, after which the transferred V-in-Mt–Cpx oxybarometer is evaluated against independently constrained experimental fO_2 values.

Its applicability to natural systems is further assessed through comparison with established mineral based oxybarometers, including the V-in-olivine and Eu-in-Cpx–Pl approaches. Finally, we investigate the influence of ilmenite exsolution from magnetite and apply the V-in-Mt–Cpx oxybarometer to the Panzhihua intrusion and the Upper Zone of the Bushveld Complex to examine contrasting redox evolution in Fe–Ti–V-bearing plutonic systems.

2. Methods

2.1 Calibrating and validation data for V partitioning models

With the aim of constructing a V-in-Mt–Cpx oxybarometer from experimentally constrained V partitioning relationships, we compiled three experimental datasets: a Cpx–melt dataset, a Mt–melt dataset, and a coexisting Mt–Cpx dataset. The Cpx–melt and Mt–melt datasets were used to calibrate forward mineral–melt V partitioning models, whereas the Mt–Cpx dataset was used to construct the transferred mineral-pair oxybarometer. A subset of experiments in which V was measured in both magnetite and clinopyroxene was reserved for independent validation of both the transferred $D_V^{Mt/Cpx}$ values and the final V-in-Mt–Cpx oxybarometer. Only experiments with well-constrained temperature, fO_2, phase compositions, V concentrations or V partition coefficients, and complete model input variables were retained. The full datasets and original references are provided in Supplementary Data S1–S3.

The Cpx–melt dataset comprises 227 experiments and was used to calibrate the Cpx–melt V partitioning model. It covers temperatures from 835 to 1900 °C and fO_2 from ΔFMQ =-4.84 to+7.19, with melt SiO_2 contents ranging from 41.56 to 73.50 wt.%. The Mt–melt dataset comprises 87 experiments and was used to calibrate the Mt–melt V partitioning model. It covers

temperatures from 1068 to 1325 °C and fO_2 from ΔFMQ= -3.83 to +4.89 with melt SiO_2 contents of 30.84–76.80 wt.% and $Na_2O + K_2O$ contents of 0–08.01 wt.%.

The Mt–Cpx dataset comprises 190 coexisting magnetite–clinopyroxene pairs and was used to construct the transferred V-in-Mt–Cpx oxybarometer. This dataset includes experimental temperatures, fO_2, clinopyroxene and magnetite major-element compositions, and melt compositional information. Because paired reliable V analyses in both magnetite and clinopyroxene are limited, $D_V^{Mt/Cpx}$values for most experiments were derived from the Cpx–melt and Mt–melt forward models using the transfer procedure described below. The Mt–Cpx dataset spans 800–1160 °C and ΔFMQ= -2.47 to +4.32 with melt SiO_2 contents of 46.64–73.59 wt.% and $Na_2O + K_2O$ contents of 2.64–11.91 wt.%.

A subset of eight experiments with measured V concentrations in both magnetite and clinopyroxene was withheld from model training and used for independent validation. These experiments were used in two ways: first, to compare measured and predicted $\log_{10} D_V^{Mt/Cpx}$; and second, to test whether the final V-in-Mt–Cpx oxybarometer can reproduce independently constrained experimental fO_2 (ΔFMQ).

The compositional coverage of the datasets was evaluated using melt total alkali–silica diagrams, magnetite $FeO–Fe_2O_3–TiO_2$ ternary diagrams, and clinopyroxene Wo–En–Fs diagrams (Fig. 1). These diagrams define the calibration range of the models and provide a basis for assessing extrapolation when the oxybarometers are applied to natural samples.

2.2 Transfer of mineral–melt V partitioning to the V-in-Mt–Cpx oxybarometer

The V-in-Mt–Cpx oxybarometer was derived by propagating experimentally calibrated mineral–melt V partitioning relationships into a mineral-pair framework. This formulation was

necessary because direct experimental constraints on V partitioning between coexisting magnetite and clinopyroxene are limited, whereas V partitioning between each mineral and silicate melt is more extensively constrained. The calibration therefore begins with Cpx–melt and Mt–melt partitioning models, which are subsequently combined to define the Mt–Cpx V partitioning term used in the final oxybarometer.

For each mineral–melt system, V partitioning was parameterized as a function of temperature, oxygen fugacity, mineral composition, and melt composition:

$$\log_{10}\left(D_{\mathrm{V}}^{i/\mathrm{melt}}\right) = F_i(T, \Delta\mathrm{FMQ}, X_i, X_{\mathrm{melt}}) \qquad (1)$$

where i denotes either Cpx or Mt, T is temperature, ΔFMQ is fO_2 relative to the FMQ buffer, and X_i and X_{melt} are the major-element compositions of the mineral and melt, respectively. Equation (1) defines two forward partitioning models: F_{Cpx}, which predicts $\log_{10} D_{\mathrm{V}}^{\mathrm{Cpx/melt}}$, and F_{Mt}, which predicts $\log_{10} D_{\mathrm{V}}^{\mathrm{Mt/melt}}$.

Because fO_2 is a primary control on V partitioning, the same mineral–melt datasets were also calibrated in inverse form:

$$\Delta\mathrm{FMQ} = G_i\left(T, X_i, X_{\mathrm{melt}}, \log_{10}\left(D_{\mathrm{V}}^{i/\mathrm{melt}}\right)\right) \qquad (2)$$

where G_i represents the V-in-Cpx and V-in-Mt mineral–melt oxybarometers. These inverse models provide reference oxybarometers for systems in which equilibrium melt compositions are preserved or can be independently constrained. They are derived from the same experimental relationships as the forward models, but the construction of the V-in-Mt–Cpx oxybarometer relies specifically on the forward partitioning models F_{Cpx} and F_{Mt}.

The transfer from mineral–melt to mineral-pair partitioning follows from the assumption that magnetite and clinopyroxene equilibrated with a common silicate melt. Under this

condition, the melt concentration term cancels, and the inter-mineral V partition coefficient can be expressed as the ratio of the two mineral–melt partition coefficients:

$$\log_{10}\left(D_{\mathrm{V}}^{\mathrm{Mt/Cpx}}\right) = \log_{10}\left(D_{\mathrm{V}}^{\mathrm{Mt/melt}}\right) - \log_{10}\left(D_{\mathrm{V}}^{\mathrm{Cpx/melt}}\right) \qquad (3)$$

For each experiment in the Mt–Cpx dataset, $\log_{10} D_{\mathrm{V}}^{\mathrm{Mt/melt}}$ and $\log_{10} D_{\mathrm{V}}^{\mathrm{Cpx/melt}}$ were predicted from Eq. (1) using the corresponding experimental temperature, fO_2, mineral compositions, and melt composition. The predicted mineral–melt partition coefficients were then combined using Eq. (3) to obtain model-derived $\log_{10} D_{\mathrm{V}}^{\mathrm{Mt/Cpx}}$ values. This procedure converts the Mt–Cpx experimental dataset into a transferred training dataset with a complete mineral-pair V partitioning variable.

The final V-in-Mt–Cpx oxybarometer was calibrated using temperature, mineral compositions, and the transferred Mt–Cpx partitioning term:

$$\Delta\mathrm{FMQ} = H\left(T, X_{\mathrm{Cpx}}, X_{\mathrm{Mt}}, \log_{10}\left(D_{\mathrm{V}}^{\mathrm{Mt/Cpx}}\right)\right) \qquad (4)$$

where X_{Cpx} and X_{Mt} are the major-element compositions of clinopyroxene and magnetite, respectively. During calibration, $\log_{10} D_{\mathrm{V}}^{\mathrm{Mt/Cpx}}$ was derived from the two mineral–melt forward models. For natural samples and independent validation experiments in which V was measured in both minerals, the same term was calculated directly from measured V concentrations:

$$\log_{10}\left(D_{\mathrm{V}}^{\mathrm{Mt/Cpx}}\right) = \log_{10}\left(\frac{C_{\mathrm{V}}^{\mathrm{Mt}}}{C_{\mathrm{V}}^{\mathrm{Cpx}}}\right) \qquad (5)$$

where $C_{\mathrm{V}}^{\mathrm{Mt}}$ and $C_{\mathrm{V}}^{\mathrm{Cpx}}$ are the V concentrations in magnetite and clinopyroxene, respectively. This formulation preserves the experimental basis of mineral–melt V partitioning while replacing the melt-dependent input with a directly measurable mineral-pair variable, allowing

187 the oxybarometer to be applied to plutonic rocks using mineral compositions, mineral V
188 concentrations, and an independent temperature estimate.

189 **2.3. Machine-learning workflow and model interpretation**

190 All forward partitioning models and inverse fO_2 models were calibrated using a consistent
191 machine-learning workflow. Four algorithms were tested: support vector regression, decision
192 trees, random forests, and CatBoost (Cortes and Vapnik 1995, Breiman 2001, Breiman et al.
193 2017, Prokhorenkova et al. 2019). These algorithms were selected to compare models with
194 different degrees of flexibility and to evaluate their ability to capture nonlinear relationships
195 among temperature, phase composition, V partitioning, and fO_2. For each dataset, the data were
196 divided into training and test subsets using an 80:20 ratio. The training subset was used for
197 model fitting, cross-validation, and hyperparameter optimization, whereas the test subset was
198 reserved for final performance evaluation. Depending on dataset size, either 10-fold or 3-fold
199 cross-validation was applied(Hastie et al. 2009). Hyperparameters were optimized by grid
200 search. Model performance was evaluated using the coefficient of determination, R^2, and root
201 mean squared error, RMSE(Okoye and Hosseini 2024).

202 For scale-sensitive algorithms, such as support vector regression, input variables were
203 standardized using parameters fitted only on the training subset, and the same transformation
204 was then applied to the test subset. Tree-based algorithms, including decision trees, random
205 forests, and CatBoost, were trained using unscaled input variables(Cortes and Vapnik 1995,
206 Breiman 2001, Hastie et al. 2009, Breiman et al. 2017, Prokhorenkova et al. 2019). All
207 preprocessing steps were fitted only on the training data to avoid information leakage.

Because experimental petrology datasets are commonly small, model performance was also tested using different random splits. Final models were selected by jointly considering cross-validation performance, independent test-set performance, stability across random splits, and geochemical interpretability. When several algorithms produced similar statistical performance, preference was given to the model that yielded stable predictions and feature responses consistent with known controls on V partitioning.

Feature-importance and SHAP analyses were used to evaluate the relative influence of input variables on model predictions(Lundberg et al. 2020). SHAP is an interpretability method that shows how each feature contributes to model predictions(Lundberg and Lee 2017). These analyses were used to assess whether the models were mainly controlled by geochemically meaningful variables, especially V partition coefficients, temperature, and phase compositions, rather than by incidental correlations in the datasets. All models were implemented in Python using scikit-learn and CatBoost. The datasets, optimized parameters, and scripts used for model training and prediction are provided in the Supplementary Materials.

2.4 Experimental and natural sample validation

The model framework was evaluated through a sequence of partitioning, experimental, and natural-sample tests. First, the transfer from mineral–melt to mineral-pair partitioning was assessed using the eight independent Mt–Cpx experiments in which V was measured in both magnetite and clinopyroxene. For these experiments, measured $\log_{10} D_{\mathrm{V}}^{\mathrm{Mt/Cpx}}$ values were calculated using Eq. (5) and compared with values predicted by combining the Cpx–melt and Mt–melt forward models using Eq. (3).

The same experiments were then used to test the final V-in-Mt–Cpx oxybarometer. For each experiment, $\log_{10} D_V^{Mt/Cpx}$ was calculated directly from the measured V concentrations in magnetite and clinopyroxene, and fO_2 was calculated using Eq. (4). The calculated values were compared with the independently constrained experimental fO_2. This validation provides a direct test of whether the transferred mineral-pair model can reproduce experimental fO_2, rather than only mineral-pair V partitioning.

For natural samples, crystallization temperatures were estimated using a previously calibrated clinopyroxene thermometer(Chicchi et al. 2023). These temperatures were used as input parameters for all V-based oxybarometers. For mineral–melt calculations, reconstructed equilibrium melt compositions were used together with clinopyroxene compositions in the temperature calculation, whereas the V-in-Mt–Cpx oxybarometer required only the clinopyroxene-based temperature estimate and measured mineral compositions. Samples yielding temperatures outside the calibration range of the V-partitioning models were excluded from subsequent fO_2 calculations.

Natural sample validation was carried out using independent mineral-based redox constraints. For picrite samples from the Emeishan Large Igneous Province, fO_2 values calculated using the V-in-Cpx oxybarometer were compared with those obtained from a V-in-olivine oxybarometer. For mid-ocean-ridge gabbros, fO_2 values calculated using the V-in-Mt–Cpx oxybarometer were compared with estimates from the Eu-in-Cpx–Pl oxybarometer. Published data from the Panzhihua layered intrusion were also used to compare results from the V-in-Cpx, V-in-Mt, and V-in-Mt–Cpx oxybarometers.

For applications of the mineral–melt inverse models to natural samples, equilibrium melt compositions were constrained before calculating fO_2. Where quenched melts were

unavailable, melt compositions were reconstructed from whole-rock compositions by adding or subtracting olivine components until Fe–Mg exchange equilibrium was reached between the reconstructed melt and the analyzed minerals. For clinopyroxene-based calculations, the reconstructed melt was adjusted to satisfy $K_D^{\mathrm{Fe-Mg}}$ (Cpx–melt) =0.27 whereas for olivine-based reference calculations it was adjusted to satisfy $K_D^{\mathrm{Fe-Mg}}$ (Ol–melt) =0.34 This procedure provides an internally consistent estimate of the melt composition in equilibrium with the analyzed mineral, rather than assuming that the measured whole-rock composition directly represents the equilibrium liquid.

Uncertainty propagation was performed by perturbing model input variables within realistic analytical and petrological uncertainties and recalculating ΔFMQ. Perturbed variables included V partition coefficients, mineral or melt major-element compositions, and temperature. The resulting distributions of predicted ΔFMQ were used to evaluate the sensitivity of each oxybarometer to input uncertainty.

2.5 Exsolution sensitivity and application to layered intrusions

The effect of ilmenite exsolution from magnetite on calculated fO_2 was evaluated by mass-balance correction of magnetite compositions. For each oxide or trace element component j, the pre-exsolution magnetite composition was estimated as:

$$C_0^j = X_{\mathrm{Mt}} C_{\mathrm{Mt}}^j + X_{\mathrm{Ilm}} C_{\mathrm{Ilm}}^j \qquad (6)$$

where C_0^j is the reconstructed pre-exsolution composition, C_{Mt}^j and C_{Ilm}^j are the compositions of residual magnetite and exsolved ilmenite, and $X_{\mathrm{Mt}}$and $X_{\mathrm{Ilm}}$are their modal fractions, with $X_{\mathrm{Mt}} + X_{\mathrm{Ilm}} = 1$. Ilmenite compositions were taken from measured lamellae where available, or from representative published analyses of ilmenite exsolution lamellae in

274 comparable layered mafic intrusions. The range of X_{Ilm} was chosen to cover observed or
275 petrographically reasonable exsolution proportions.

276 For each corrected magnetite composition, fO_2 was recalculated using the V-in-Mt–Cpx
277 oxybarometer while keeping clinopyroxene composition and temperature fixed. This procedure
278 isolates the effect of magnetite modification on the recovered fO_2.

279 The V-in-Mt–Cpx oxybarometer was then applied to coexisting magnetite and
280 clinopyroxene from the Panzhihua and Bushveld layered intrusions. For each mineral pair,
281 $\log_{10} D_{\mathrm{V}}^{\mathrm{Mt/Cpx}}$ was calculated directly from measured V concentrations, and fO_2 was calculated
282 using measured mineral compositions and clinopyroxene-based temperature estimates. Only
283 texturally associated Mt–Cpx pairs with compositions within, or close to, the experimental
284 calibration range were retained. Analyses showing alteration, secondary replacement, strong
285 exsolution-related disturbance, or anomalous trace-element behavior were excluded. Calculated
286 fO_2 values were grouped by sample and stratigraphic position for comparison between
287 intrusions.

288 **3. Results**

289 **3.1 Mineral–melt V partitioning models and associated inverse oxybarometers**

290 Among the algorithms calibrated for Cpx–melt V partitioning, CatBoost gives the lowest
291 prediction error. The selected model closely reproduces experimental $\log_{10} D_{\mathrm{V}}^{\mathrm{Cpx/melt}}$, with an
292 R^2 of 0.97 and an RMSE of 0.01 log units on the test dataset (Fig. 2a; Table 1). Predicted values
293 are distributed around the 1:1 line across the calibration range, and residuals remain centered
294 near zero without systematic variation with fO_2 (ΔFMQ) temperature, melt composition, or

clinopyroxene composition. Feature importance and SHAP analyses rank ΔFMQ, melt SiO_2, melt CaO, and clinopyroxene Mg# among the principal controls on $D_V^{Cpx/melt}$ (Fig. 5a). The SHAP dependence of fO_2 (ΔFMQ) is negative, showing that more oxidizing conditions generally reduce V partitioning into clinopyroxene. Temperature and compositional variables contribute smaller but systematic effects, consistent with the dependence of Cpx–melt V partitioning on both V valence state and crystal–melt chemistry.

When the Cpx–melt dataset is calibrated in inverse form, CatBoost also yields the most accurate V-in-Cpx oxybarometer. The model predicts experimental fO_2 (ΔFMQ) with an R^2 of 0.99 and an RMSE of 0.39 ΔFMQ units on the test dataset (Fig. 2b; Table 1). Most predictions lie close to the 1:1 line, although the largest residuals occur near the reduced and oxidized limits of the calibration range. In the SHAP analysis, $\log_{10} D_V^{Cpx/melt}$ is the dominant predictor, followed by temperature and selected melt and clinopyroxene compositional variables (Fig. 5b). The inverse model therefore uses the V partition coefficient as the main redox-sensitive variable: higher $\log_{10} D_V^{Cpx/melt}$ corresponds to lower calculated fO_2 (ΔFMQ), whereas compositional terms account for variations in clinopyroxene–melt equilibrium.

The Mt–melt forward calibration is best represented by CatBoost. This model reproduces experimental $\log_{10} D_V^{Mt/melt}$ with an R^2 of 0.98 and an RMSE of 0.13 log units on the test dataset (Fig. 3a; Table 1). It accounts for the large range of magnetite–melt V partition coefficients, including both reduced and oxidized experiments, and residuals show no clear dependence on fO_2 (ΔFMQ), melt composition, or magnetite composition. SHAP results identify fO_2 (ΔFMQ), magnetite TiO_2, Fe components, and melt composition as the main variables controlling $D_V^{Mt/melt}$ (Fig. 6a). As in the Cpx–melt model, increasing fO_2 (ΔFMQ) generally lowers predicted $D_V^{Mt/melt}$, reflecting the lower compatibility of oxidized V species.

The additional influence of Ti and Fe components indicates that spinel solid solution and site occupancy also affect V incorporation into magnetite.

The inverse Mt–melt calibration defines the V-in-Mt oxybarometer, for which CatBoost gives the lowest prediction error. The model predicts experimental ΔFMQwith an $R^2$of 0.99 and an RMSE of 0.18 fO_2 (ΔFMQ) on the test dataset (Fig. 3b; Table 1), with slightly less scatter than the V-in-Cpx oxybarometer. SHAP values show that $\log_{10} D_V^{Mt/melt}$ dominates the prediction, whereas temperature and magnetite compositional variables provide secondary corrections (Fig. 6b). The negative dependence of calculatedfO_2 (ΔFMQ) an $\log_{10} D_V^{Mt/melt}$is consistent with redox-controlled V partitioning into magnetite. Together, the two forward mineral–melt models provide the quantitative inputs needed to calculate transferred $\log_{10} D_V^{Mt/Cpx}$, whereas the V-in-Cpx and V-in-Mt oxybarometers serve as associated mineral–melt reference models for samples with constrained equilibrium melt compositions.

3.2 Calibration and feature controls of the transferred V-in-Mt–Cpx oxybarometer

The calibrated Cpx–melt and Mt–melt forward models were coupled to calculate transferred $\log_{10} D_V^{Mt/Cpx}$values for the Mt–Cpx experimental dataset. For each experiment, predicted $\log_{10} D_V^{Mt/melt}$ and $\log_{10} D_V^{Cpx/melt}$ were combined according to Eq. (3). The resulting transferred partition coefficients span a broad range and vary systematically with experimental fO_2 (ΔFMQ), indicating that the redox dependence captured by the two mineral–melt models is retained after conversion to the mineral-pair form. The transferred Mt–Cpx dataset was then used to calibrate the final V-in-Mt–Cpx oxybarometer. CatBoost gives the best performance for this model, predicting experimental fO_2 (ΔFMQ) with an $R^2$of 0.98 and an RMSE of 0.18 ΔFMQ units on the test dataset (Fig. 4; Table 1). Predicted values closely follow

the experimental values from reduced to oxidized conditions, and residuals are centered near zero.

SHAP analysis identifies $\log_{10} D_V^{Mt/Cpx}$ as the dominant predictor in the final oxybarometer (Fig.7). This result is important because the model output is controlled primarily by the measured mineral-pair V partitioning term, rather than by mineral major-element composition alone. Temperature is the next most influential variable, followed by magnetite TiO_2, magnetite Fe components, and clinopyroxene compositional parameters such as CaO and Al_2O_3. These variables provide secondary corrections for crystal-chemical effects that influence V incorporation into the two minerals.

The dependence of ΔFMQ on the Mt–Cpx partitioning term differs from that observed in the mineral–melt inverse oxybarometers. In the V-in-Cpx and V-in-Mt models, higher mineral–melt D_V values correspond to lower calculated fO_2. In contrast, the V-in-Mt–Cpx oxybarometer shows a positive dependence on $\log_{10} D_V^{Mt/Cpx}$ (Fig. 7). This behavior reflects the ratio form of $D_V^{Mt/Cpx}$, which records the relative change in V compatibility between magnetite and clinopyroxene as redox conditions vary. The feature-response pattern therefore confirms that the final model transfers redox information from the two mineral–melt systems into a mineral-pair variable that can be measured directly in plutonic rocks.

Overall, the transferred V-in-Mt–Cpx model combines high predictive accuracy with a geochemically interpretable feature structure. Its dominant dependence on $\log_{10} D_V^{Mt/Cpx}$, together with secondary temperature and mineral-compositional effects, indicates that the model recovers fO_2 chiefly from inter-mineral V partitioning while accounting for variations in mineral chemistry.

3.3 Model validation using experimental and natural samples

The transfer from mineral–melt to mineral-pair partitioning was evaluated independently using eight experiments in which V concentrations were measured in both magnetite and clinopyroxene. For these experiments, measured $\log_{10} D_{\mathrm{V}}^{\mathrm{Mt/Cpx}}$ values were calculated directly from the mineral V concentrations and compared with values predicted by combining the Cpx–melt and Mt–melt forward models. The predicted and measured values are closely matched, with a mean residual of 0.014 log units and no systematic offset across the validation dataset (Fig. 8a). Only 8 experiments show larger deviations, and these deviations remain small relative to the full range of $\log_{10} D_{\mathrm{V}}^{\mathrm{Mt/Cpx}}$ represented by the calibration data.

The same experiments provide a direct test of the final V-in-Mt–Cpx oxybarometer. Using measured mineral V concentrations to calculate $\log_{10} D_{\mathrm{V}}^{\mathrm{Mt/Cpx}}$, the model reproduces independently constrained experimental $\Delta\mathrm{FMQ}$ values within ± 0.5 log units for six of the eight experiments (Fig. 8b). The experiment with larger discrepancies does not define a consistent positive or negative offset. Thus, the independent experimental tests support both the transfer of $D_{\mathrm{V}}^{\mathrm{Mt/Cpx}}$ from mineral–melt partitioning models and the ability of the final mineral-pair oxybarometer to recover experimental redox conditions.

Natural sample comparisons provide an additional assessment of model applicability beyond the calibration experiments. For Emeishan picrites, fO_2 (ΔFMQ) values calculated using the V-in-Cpx oxybarometer are broadly consistent with those obtained from the V-in-olivine oxybarometer, with an average difference of approximately 0.5 ΔFMQunits (Fig. 9a). For mid-ocean-ridge gabbro, the V-in-Mt–Cpx oxybarometer yields fO_2 (ΔFMQ) values that agree with estimates from the Eu-in-Cpx–Pl oxybarometer within approximately 0.2 log units (Fig. 9b).

Published samples from the Panzhihua intrusion also show comparable results among the V-in-Cpx, V-in-Mt, and V-in-Mt–Cpx oxybarometers (Fig. 9c). These comparisons indicate that the V-based models give redox estimates consistent with independent mineral-based oxybarometers in chemically diverse natural systems.

3.4 Uncertainty propagation and effect of ilmenite exsolution

Uncertainty propagation shows that analytical and petrological uncertainties lead to typical uncertainties of approximately ±0.11 to ±0.21 ΔFMQ units, depending on the model and sample type (Fig. S1). The largest contribution comes from uncertainty in V concentrations and, consequently, in calculated V partition coefficients. Temperature uncertainty produces a smaller but still measurable effect, particularly for samples close to the margins of the calibration range. In contrast, uncertainties in major-element compositions of clinopyroxene, magnetite, and reconstructed melts generally have more limited effects on calculated fO_2.

The propagated uncertainties are similar in magnitude for the three V-based oxybarometers, but their dominant error sources differ slightly. The mineral–melt oxybarometers are sensitive to uncertainties in reconstructed melt compositions as well as mineral–melt V partition coefficients. By contrast, the V-in-Mt–Cpx oxybarometer is controlled mainly by the measured inter-mineral V ratio and temperature. This difference reflects the advantage of the mineral-pair formulation for plutonic rocks: it removes the need to reconstruct melt composition, while still retaining sensitivity to redox-dependent V partitioning.

Mass balance simulations were used to evaluate the extent to which ilmenite exsolution from magnetite may bias oxygen fugacity estimates obtained using the V in clinopyroxene and

406 magnetite oxybarometer. Within the modeled exsolution boundary, defined by residual
407 magnetite compositions with TiO_2, fO_2. values calculated from exsolved magnetite are typically
408 lower than those reconstructed for magnetite before exsolution by approximately 0.25 to 0.35
409 ΔFMQ, and the maximum deviation does not exceed about 0.4 ΔFMQ (Fig. S2). These changes
410 remain smaller than the uncertainty of ±0.5 ΔFMQ, indicating that ilmenite exsolution within
411 the simulated compositional range does not exert a dominant influence on the recovered redox
412 signal. The fO_2 estimates presented in the application section are therefore considered
413 geologically meaningful, provided that the effects of exsolution remain within the modeled
414 boundary and smaller than the overall analytical and model uncertainty. Magnetite
415 compositions beyond this boundary, especially those approaching complete Ti depletion,
416 should be excluded or interpreted with caution.

417 **3.5 Redox estimates for the Panzhihua intrusion and the Upper Zone of the Bushveld**
418 **Complex**

419 The V-in-Mt–Cpx oxybarometer was applied to coexisting magnetite and clinopyroxene
420 from the Panzhihua intrusion and the Upper Zone of the Bushveld Complex to evaluate redox
421 variations in Fe–Ti–V-bearing plutonic systems. Panzhihua samples yield consistently oxidized
422 values, with calculated fO_2 (ΔFMQ) ranging from approximately +1.29 to +1.99(Fig. 10a). The
423 within-sample variation is generally limited, and calculated fO_2 shows only a weak correlation
424 with clinopyroxene Mg# ($R^2 = 0.083$; Fig. 10c). These results indicate a relatively restricted
425 range of redox conditions recorded by Mt–Cpx pairs in the analyzed Panzhihua samples.

426 Bushveld samples define a broader range of redox estimates. Calculated fO_2 (ΔFMQ)
427 values range from approximately +0.06 to +1.31(Fig. 10d), extending to lower oxygen fugacity

than the Panzhihua dataset. In contrast to Panzhihua, Bushveld samples show a clearer relationship between fO_2 and clinopyroxene Mg#, with lower Mg# generally associated with lower calculated fO_2 ($R^2 = 0.773$; Fig. 10f). The calculated values also vary more strongly with stratigraphic position, indicating greater redox heterogeneity within the sampled Bushveld section.

Discussion

4.1 Clinopyroxene–melt V partitioning and the V-in-Cpx oxybarometer

The Cpx–melt calibration confirms that V partitioning into clinopyroxene provides a quantifiable redox signal, but also shows that this signal is modulated by temperature and crystal–melt chemistry. The decrease in $D_V^{Cpx/melt}$ with increasing fO_2 is consistent with the multivalent behavior of V in silicate melts(Toplis and Corgne 2002, Mallmann and O'Neill 2009, 2013, Davis et al. 2013, Wang et al. 2019, Leuthold et al. 2023). Under relatively reduced conditions, lower-valence V species are more compatible in clinopyroxene, whereas oxidation increases the proportion of higher-valence species that are less readily incorporated into the clinopyroxene structure(Toplis and Corgne 2002, Berndt 2004, Wang et al. 2019, Holycross and Cottrell 2022*b*, Shepherd et al. 2022*a*). This redox dependence provides the basis for a Cpx–melt V oxybarometer, but the SHAP results indicate that it cannot be treated as a simple one-variable relationship.

The importance of temperature, melt SiO_2, melt CaO, and clinopyroxene Mg# indicates that Cpx–melt V partitioning reflects coupled controls from melt structure, crystal chemistry, and V valence state (Fig.5a) (Berndt 2004, Brugger and Hammer 2010, Bédard 2010, Wang et

449 al. 2019, Holycross and Cottrell 2022*b*, Shepherd et al. 2022*b*). This is where the machine-
450 learning calibration improves on conventional empirical l formulations. Regressions require the
451 functional dependence on fO_2 temperature, and composition to be specified in advance, and
452 interactions among these variables are commonly simplified or omitted In contrast, the
453 machine-learning model can accommodate nonlinear and compositional effects without
454 imposing a predetermined equation form (Higgins et al. 2022, Chicchi et al. 2023, Zou et al.
455 2024). Its value, however, does not come simply from statistical flexibility. The SHAP response
456 of fO_2 and the secondary roles of temperature and composition are consistent with expected
457 partitioning behavior, providing a geochemical check on the model structure.

458 The inverse V-in-Cpx oxybarometer demonstrates that the redox information encoded in
459 $D_V^{Cpx/melt}$ can be recovered when the equilibrium melt composition is known or can be
460 independently constrained (Fig.2b). The dominance of $\log_{10} D_V^{Cpx/melt}$ in the SHAP analysis is
461 important because it shows that the inverse model is controlled primarily by the redox-sensitive
462 V partitioning term, rather than by indirect correlations in melt or clinopyroxene major-element
463 composition (Fig.5b). Temperature and compositional variables act as corrections for crystal–
464 melt equilibrium, allowing the same partitioning signal to be applied across a broader
465 experimental compositional range.

466 The practical applicability of the V-in-Cpx oxybarometer is supported by its comparison
467 with an independent V-in-olivine oxybarometer(Wang et al. 2025*a*) for Emeishan picrites
468 (Fig.9a). The two approaches give broadly consistent fO_2 estimates, indicating that the
469 clinopyroxene-based model can recover redox conditions in natural mafic systems when the
470 equilibrium melt composition can be reasonably constrained. This comparison is important
471 because it tests the model outside the experimental calibration workflow and against an

472 independent mineral-based redox proxy. The V-in-Cpx oxybarometer is therefore useful for
473 volcanic rocks, melt-inclusion-bearing samples, and natural systems in which equilibrium melts
474 can be estimated with confidence(Toplis and Corgne 2002, Li 2018, Holycross and Cottrell
475 2022*b*, Shepherd et al. 2022*a*).

476 Its main limitation is the dependence on melt composition. In plutonic and cumulate rocks,
477 whole-rock compositions may reflect crystal accumulation, trapped liquid, and post-cumulus
478 modification rather than equilibrium liquids(Holness et al. 2007, Namur et al. 2013, Leuthold
479 et al. 2014, Charlier et al. 2015). Melt reconstruction can extend the applicability of the model,
480 but it also introduces uncertainty that may be difficult to quantify. The V-in-Cpx oxybarometer
481 is therefore best viewed as a robust mineral–melt reference model and as one experimentally
482 calibrated component of the broader transfer framework, rather than as the primary solution for
483 melt-absent plutonic rocks.

484 **4.2 Magnetite–melt V partitioning and the V-in-Mt oxybarometer**

485 Magnetite provides a more sensitive, but also more mineralogically complex, record of
486 V partitioning. As a major host of V in mafic systems, magnetite incorporates V through
487 substitutions in the spinel structure, and its V content responds to both oxygen fugacity and
488 oxide solid solution(Toplis and Corgne 2002, Sossi et al. 2018, Shepherd et al. 2022*a*). The
489 Mt–melt model captures the expected decrease in $D_V^{Mt/melt}$ with increasing fO_2 reflecting the
490 lower compatibility of oxidized V species relative to reduced V in magnetite(Toplis and Carroll
491 1995, Andújar et al. 2016, Sossi et al. 2018, Sievwright et al. 2020).

492 The SHAP structure further shows that magnetite–melt V partitioning cannot be
493 represented fully by fO_2 alone (Fig.6b). Magnetite TiO_2 and Fe components are among the

494 principal model variables, indicating that spinel solid solution, cation distribution, and site
495 availability exert important controls on V incorporation(Buddington and Lindsley 1964,
496 Backhaus-Ricoult and Dieckmann 1986, Van Orman and Crispin 2010). These effects are
497 difficult to capture with simple empirical regressions, particularly across experiments involving
498 variable melt compositions, magnetite compositions, and redox conditions. The machine-
499 learning calibration therefore provides a more flexible description of this multivariate behavior
500 while retaining geochemical interpretability through the feature structure.

501 The inverse V-in-Mt oxybarometer benefits from the strong sensitivity of $D_V^{Mt/melt}$ to
502 oxygen fugacity(Toplis and Corgne 2002, Sossi et al. 2018, Shepherd et al. 2022*a*). Its SHAP
503 pattern shows that the model is governed primarily by the mineral–melt V partition coefficient,
504 with temperature and magnetite composition providing secondary corrections (Fig.6a). This
505 behavior supports the use of magnetite–melt V partitioning as a quantitative redox proxy where
506 melt compositions are constrained. Compared with empirical oxide-based calibrations that
507 depend mainly on major-element exchange, the V-in-Mt model uses $D_V^{Mt/melt}$ signal and can
508 be adjusted for oxide composition through the machine-learning framework.

509 The practical utility of the V-in-Mt oxybarometer is supported by its consistency with
510 the V-in-Cpx and V-in-Mt–Cpx models in the Panzhihua dataset (Fig.9c). Although this
511 comparison is not as independent as the experimental Mt–Cpx validation, it provides a useful
512 natural sample check because the three oxybarometers use different input structures: Cpx–melt,
513 Mt–melt, and Mt–Cpx. Their broadly comparable results suggest that the V-in-Mt model can
514 yield realistic redox estimates in natural Fe–Ti–V-bearing systems when magnetite
515 compositions are well preserved and equilibrium melt compositions are reasonably constrained.

For plutonic rocks, however, the same limitations that affect another mineral–melt oxybarometers remain. Equilibrium melts are rarely preserved, and reconstructed melt compositions may be uncertain in cumulate systems. Magnetite also requires additional caution because it can be modified by ilmenite exsolution, oxidation, alteration, and subsolidus re-equilibration(Wei et al. 2020, Brzozowski et al. 2021, Hou et al. 2021, Wang et al. 2025*b*). Our exsolution calculations indicate that moderate ilmenite exsolution generally introduces deviations smaller than the propagated uncertainty of the V-in-Mt–Cpx oxybarometer, although petrographic screening remains essential. Magnetite grains showing extensive exsolution, alteration, or compositional heterogeneity should not be regarded as preserving primary magmatic compositions. In this study, the Mt–melt calibration therefore serves two roles: it provides a standalone mineral–melt oxybarometer for suitable samples, and more importantly, it supplies the magnetite-side partitioning term required to construct the melt-independent Mt–Cpx model.

4.3 Transfer of V partitioning to a melt-independent Mt–Cpx oxybarometer

The V-in-Cpx–Mt oxybarometer transfers the experimentally calibrated V–fO_2 relationship from mineral–melt systems to a directly measurable mineral-pair framework. When Mt, Cpx, and melt are in equilibrium, the inter-mineral V partition coefficient can be expressed as:

$$D_V^{Mt/Cpx} = \frac{D_V^{Mt/melt}}{D_V^{Cpx/melt}}$$

This formulation eliminates the explicit melt term, allowing the redox information originally recorded by Mt/Cpx–melt partitioning to be inherited by the coexisting Mt–Cpx assemblage(Mallmann and O'Neill 2009, Papike et al. 2013, Holycross and Cottrell 2022*a*,

Shepherd et al. 2022*b*, Dygert et al. 2025). The resulting oxybarometer therefore retains the experimental basis of V partitioning while avoiding the need to reconstruct equilibrium melt compositions in natural cumulates.

This framework differs from a purely empirical mineral-pair regression in several ways. First, the transferred variable is grounded in mineral–melt partitioning relationships that have explicit experimental redox dependence(Mallmann and O'Neill 2009, Shepherd et al. 2022*b*). Second, the machine-learning calibration allows the final oxybarometer to account for nonlinear effects of temperature and mineral chemistry, rather than forcing the data into a prescribed linear or polynomial form (Zou et al. 2024; Wang et al. 2025). Third, the final V-in-Mt–Cpx model removes the most problematic input for plutonic rocks: equilibrium melt composition. The model therefore retains the experimental basis of mineral–melt V partitioning while replacing melt-dependent inputs with directly measured mineral compositions and C_V^{Mt}/C_V^{Cpx}.

The SHAP feature hierarchy closely mirrors the established geochemical controls on V partitioning (Fig. 7). The dominant importance of $\log_{10} D_V^{Mt/Cpx}$ reflects the fact that inter-mineral V partitioning carries the primary redox signal. Because V is multivalent, changes in fO_2 systematically modify its valence state and thus its relative compatibility between magnetite and clinopyroxene (Toplis and Corgne, 2002; Mallmann and O'Neill, 2009, 2013; Leuthold et al., 2023). Consequently, the model derives most of its predictive power from the experimentally constrained response of $D_V^{Mt/Cpx}$ to fO_2 rather than empirical correlations among major elements. The remaining predictors mainly account for crystal-chemical effects on V partitioning. Magnetite FeO is the most influential compositional variable because it reflects Fe^{2+}–Fe^{3+} systematics and spinel stoichiometry, both of which govern charge balance

and V incorporation (Buddington and Lindsley 1964, Backhaus-Ricoult and Dieckmann 1986, Van Orman and Crispin 2010). Magnetite Al_2O_3 and MgO, together with clinopyroxene Al_2O_3, MgO, and CaO, reflect variations in spinel solid solution, Tschermak substitution, and cation site occupancy that modify V compatibility in the two minerals (Papike 2005, Shepherd et al. 2022*a*) Rather than directly recording fO_2, these variables constrain the crystal-chemical environment in which V partitioning occurs, allowing the model to isolate the redox signal carried by $D_V^{Mt/Cpx}$.

The generalizability of the V-in-Mt–Cpx oxybarometer is supported at three levels. Statistical generalization is indicated by cross-validation and repeated train–test splits, which show that model performance is not tied to a single partition of the experimental data. Experimental generalization is provided by paired Mt–Cpx experiments with measured V in both minerals. In these experiments, predicted and measured $D_V^{Mt/Cpx}$agree closely, and the final oxybarometer reproduces independently constrained ΔFMQfor most experiments within uncertainty. Petrological generalization is indicated by natural-sample comparisons with independent mineral-based oxybarometers, including V-in-olivine and Eu-in-Cpx–Pl approaches. These tests are critical because high accuracy on a calibration dataset alone would not demonstrate that the model can be applied to natural intrusive rocks.

The natural-sample tests also clarify the practical niche of the Mt–Cpx oxybarometer. Its agreement with the Eu-in-Cpx–Pl oxybarometer(Dygert et al. 2025) in mid-ocean-ridge gabbro's supports its use in melt-absent plutonic rocks where independent mineral-pair redox constraints are available. Its consistency with the V-in-Cpx and V-in-Mt models in Panzhihua further suggests that the transferred mineral-pair model can recover redox conditions comparable to those obtained from mineral–melt approaches, while avoiding the need to specify

584 an equilibrium melt. This is the main practical advantage of the model: it converts
585 experimentally calibrated mineral–melt V partitioning into a form that can be applied directly
586 to coexisting minerals in cumulate rocks.

587 The model nevertheless has defined application limits. It should be applied to texturally
588 associated magnetite–clinopyroxene pairs that plausibly crystallized from, or equilibrated with,
589 the same melt domain(Papike et al. 2013). Reliable temperature estimates are required, and
590 samples should lie within or near the experimental calibration range in terms of temperature
591 and mineral composition. Accurate determination of V concentrations in both minerals is
592 essential because $D_V^{Mt/Cpx}$is the dominant predictor of the V-in-Mt–Cpx oxybarometer (Fig. 7).
593 Mineral pairs affected by extensive alteration, secondary oxidation of magnetite, or lacking
594 petrographic evidence for equilibrium should be excluded. Finally, SHAP analyses are intended
595 to aid geochemical interpretation of the calibrated models rather than establish causal
596 relationships; they evaluate whether model responses are consistent with current geochemical
597 understanding but should always be interpreted alongside petrographic observations and
598 experimental constraints.

599 Within these boundaries, the V-in-Mt–Cpx oxybarometer provides a practical advantage
600 over both conventional Fe–Ti oxide oxybarometry and mineral–melt V oxybarometers. Fe–Ti
601 oxide equilibria may be reset during cooling and can record late subsolidus conditions rather
602 than magmatic fO_2(Lattard et al. 2012, Loucks et al. 2018, Hou et al. 2021). Mineral–melt
603 oxybarometers retain direct experimental meaning but require melt compositions that are often
604 unavailable in plutonic rocks(Arató and Audétat 2017*b*, *a*, Shepherd et al. 2022*b*, Dygert et al.
605 2025). The Mt–Cpx V partitioning approach occupies the middle ground: it uses an
606 experimentally transferred partitioning framework, but its final inputs are mineral-based. This

607 makes it especially useful for layered intrusions and other cumulate systems in which magmatic
608 redox information must be extracted from preserved minerals rather than from melts(Charlier
609 et al. 2015, Dygert et al. 2025).

610 **4.4 Redox characteristics of the Panzhihua intrusion and the Upper Zone of the Bushveld**
611 **Complex**

612 Application of the V in Cpx–Mt oxybarometer to the Panzhihua and Bushveld layered
613 intrusions reveals two contrasting redox evolution paths in deep seated mafic–ultramafic
614 magmatic systems The Panzhihua drill core spans the Lower, Middle, and Upper Zones and
615 records the principal Fe–Ti oxide mineralization framework of the intrusion (Chen et al. 2017),
616 whereas the Bushveld Bellevue drill core covers key intervals of the Upper Zones with
617 continuous lithological, stratigraphic, and mineral-chemical constraints (Ashwal et al.2005).

618 In the Upper Zone of the Bushveld Complex, calculated fO_2 decreases systematically with
619 decreasing Cpx Mg# (Fig. 10f), indicating reduction coupled to magmatic differentiation. This
620 trend is consistent with models in which Upper Zone evolved largely through prolonged
621 fractional crystallization of Fe-rich residual melts, with local recharge, mixing, melt percolation,
622 and cyclicity superimposed on this evolution (Tegner et al. 2006; VanTongeren and Mathez
623 2012; Namur et al. 2013; Mangwegape et al. 2016). It also agrees in direction with previous
624 Bushveld Upper Zone redox estimates based on Fe in plagioclase and Fe–Ti oxide constraints,
625 which suggest near- to below-FMQ conditions and, in some cases, decreasing fO_2 with
626 fractionation (Tegner et al. 2002; Lundgaard and Tegner 2004; Tegner and Cawthorn 2010).
627 Because different oxybarometers may record different minerals, crystallization intervals, and
628 closure temperatures, this agreement is most meaningful in terms of trend rather than absolute

value. In a relatively closed or weakly replenished system, continued Fe–Ti oxide crystallization can lower melt $Fe^{3+}/\Sigma Fe$ and apparent fO_2 while progressive Fe enrichment and development of Fe-rich residual or immiscible melts characterize the late Bushveld Upper Zone (Cawthorn and Ashwal 2009; Fischer et al. 2016; Bilenker et al. 2017; Yao et al. 2021). The V-in-Mt–Cpx results therefore support a differentiation-dominated redox trajectory for Bushveld, with intermittent open-system processes superimposed on a broadly evolving residual melt.

Panzhihua records a contrasting redox evolution. Calculated fO_2 values remain consistently high, ranging from approximately +1.4 to +1.9 ΔFMQ, throughout the drill core despite extensive Fe–Ti oxide crystallization and accumulation (Fig. 10b). These oxidation states agree well with independent estimates for the parental high-Ti picritic magmas of the ELIP, indicating that the calculated fO_2 values are geologically realistic and preserve the primary redox state of the parental magma. If oxide fractionation alone governed magma redox evolution, sustained magnetite crystallization would progressively remove Fe^{3+} from the melt, decrease the melt $Fe^{3+}/\Sigma Fe$ ratio, and drive fO_2 toward lower values during differentiation. Instead, Panzhihua shows little systematic decrease in fO_2 with decreasing Cpx Mg# or stratigraphic height (Fig. 10a, c), implying that differentiation-driven reduction was counteracted during oxide accumulation. The most consistent explanation is repeated recharge by relatively oxidized, Fe–Ti-rich magma. Reversals in augite Mg#, cyclic lithological variations, and the spatial association between cyclic units and massive Fe–Ti oxide layers have been interpreted as evidence for repeated replenishment and in situ Fe–Ti oxide crystallization within a mush-dominated system (Song et al. 2013; Luan et al. 2014; Bai et al. 2021; Wang et al. 2023). Recharge of relatively oxidized primitive magma was therefore likely the primary mechanism buffering the chamber against the redox decrease expected from progressive

652 magnetite crystallization. Assimilation of the surrounding dolomitic carbonate wall rocks may
653 have further reinforced this oxidation buffering, as carbonate assimilation has been suggested
654 to increase magma oxidation in the Panzhihua system(Ganino et al. 2008, 2013). These
655 processes provide a plausible explanation for the persistently elevated fO_2 recorded during
656 magma differentiation.

657 Together, the Upper Zone of the Bushveld Complex and Panzhihua results show that fO_2
658 volution in layered intrusions reflects the balance between differentiation-driven reduction and
659 recharge-driven oxidation buffering, rather than oxide crystallization alone. In Bushveld, the
660 V-in-Mt–Cpx results are consistent with a relatively closed, differentiation-dominated redox
661 path. In Panzhihua, persistently high fO_2 values require open-system redox buffering during
662 oxide accumulation. This distinction has direct metallogenic implications: efficient Fe–Ti–V
663 oxide mineralization may require not only oxide saturation, but also a magma-chamber redox
664 budget capable of sustaining favorable oxidation states during repeated cycles of replenishment
665 and accumulation. By extracting redox information from a directly measurable mineral pair,
666 the V-in-Mt–Cpx oxybarometer provides a way to link magmatic redox evolution with chamber
667 dynamics and ore-forming processes in plutonic Fe–Ti–V systems.

668 **Conclusions**

669 (1) A machine-learning framework was developed to quantify V partitioning and oxygen
670 fugacity in mafic magmatic systems. Experimental Cpx–melt and Mt–melt datasets were used
671 to calibrate V partitioning as a function of oxygen fugacity, temperature, mineral chemistry,
672 and melt composition. These calibrations were subsequently transferred to coexisting

magnetite–clinopyroxene pairs, establishing a melt-independent V-in-Mt–Cpx oxybarometer together with complementary V-in-Cpx and V-in-Mt oxybarometers.

(2) The calibrated models accurately reproduce experimental V partitioning and oxygen fugacity while retaining geochemical interpretability. Machine-learning models capture the nonlinear dependence of V partitioning on redox conditions, temperature, and composition without prescribing empirical functional forms. SHAP analyses indicate that V partition coefficients dominate oxygen fugacity predictions, whereas temperature and major-element compositions primarily account for equilibrium-related corrections. Validation against experimental partition coefficients, independently constrained experimental fO_2, and natural mineral-based oxybarometers demonstrates the robustness and generalizability of the proposed framework.

(3) The V-in-Mt–Cpx oxybarometer extends experimentally calibrated V partitioning oxybarometry to plutonic rocks where equilibrium melts are absent. By eliminating the need for melt compositions, the method overcomes a major limitation of existing mineral–melt oxybarometers while reducing the influence of subsolidus re-equilibration that commonly affects conventional Fe–Ti oxide oxybarometers. It therefore provides a practical tool for reconstructing magmatic redox conditions in layered intrusions and other cumulate systems.

(4) Application to the Bushveld and Panzhihua layered intrusions demonstrates the geological significance of the new oxybarometer. The Bushveld Upper Zone records progressive reduction during magmatic differentiation, whereas the Panzhihua intrusion maintained persistently oxidized conditions despite extensive Fe–Ti oxide crystallization, consistent with oxidation buffering through repeated recharge of relatively oxidized magma. These contrasting redox trajectories indicate that oxygen fugacity evolution in layered

intrusions reflects the balance between differentiation-driven reduction and recharge-driven oxidation buffering, highlighting the importance of magma dynamics in controlling Fe–Ti–V oxide mineralization.

Acknowledgments

This study was supported by the National Key R&D Program of China (2024YFC2909201), National Natural Science Foundation of China (42121003,42122024,42025301), CAS "Light of West China" Program (xbzgzdsys-202310), and Guizhou Provincial High-Level Innovation Talent program (No. GCC [2023]057).

Author contributions

Z.J.B. and G.S.W. conceived and designed the study, completed data collection and modeling, led the writing of the paper.

Declaration of Competing Interest

The authors declare that they have no competing interests.

Data and materials availability

All supplementary figures are provided in the PDF file Supplementary Figures, and the datasets supporting this study are available in the Excel file Supplementary Data. The core code of RF model is available in the Python file Supplementary Code. The oxybarometer used in this study

is available for use on the website (https://kcct6hhpfn3h5yzfpzcmqh.streamlit.app/). For access to the offline oxybarometer software, please contact the authors.

References

Alex, A.; Zajacz, Z. 2022. The solubility of Cu, Ag and Au in magmatic sulfur-bearing fluids as a function of oxygen fugacity. *Geochimica et Cosmochimica Acta* 330: 93–115.

Andersen, D.J.; Lindsley, D.H.; Davidson, P.M. 1993. QUILF: a pascal program to assess equilibria among Fe Mg Mn Ti oxides, pyroxenes, olivine, and quartz. *Computers and Geosciences* 19: 1333–1350.

Andújar, J.; Scaillet, B.; Pichavant, M.; Druitt, T.H. 2016. Generation Conditions of Dacite and Rhyodacite via the Crystallization of an Andesitic Magma. Implications for the Plumbing System at Santorini (Greece) and the Origin of Tholeiitic or Calc-alkaline Differentiation Trends in Arc Magmas. *Journal of Petrology* 57: 1887–1920.

Arató, R.; Audétat, A. 2017a. Experimental calibration of a new oxybarometer for silicic magmas based on vanadium partitioning between magnetite and silicate melt. *Geochimica et Cosmochimica Acta* 209: 284–295.

Arató, R.; Audétat, A. 2017b. FeTiMM – a new oxybarometer for mafic to felsic magmas. *Geochemical Perspectives Letters*: 19–23.

Armstrong, K.; Frost, D.J.; McCammon, C.A.; Rubie, D.C.; Boffa Ballaran, T. 2019. Deep magma ocean formation set the oxidation state of earth's mantle. *Science* 365: 903–906.

Ashwal, L.D. 2005. Magmatic stratigraphy in the Bushveld Northern Lobe: continuous geophysical and mineralogical data from the 2950 m Bellevue drillcore. *South African Journal of Geology* 108: 199–232.

Backhaus-Ricoult, M.; Dieckmann, R. 1986. Defects and cation diffusion in magnetite (VII): diffusion controlled formation of magnetite during reactions in the iron-oxygen system. *Berichte der Bunsen-Gesellschaft für Physikalische Chemie* 90: 690–698.

Bai, Z.-J.; Zhong, H.; Naldrett, A.J.; Zhu, W.-G.; Xu, G.-W. 2012. Whole-rock and mineral composition constraints on the genesis of the giant hongge fe-ti-V oxide deposit in the emeishan large igneous province, southwest China. *Economic Geology* 107: 507–524.

Bai, Z.-J.; Zhong, H.; Zhu, W.-G.; Hu, W.-J.; Chen, C.-J. 2019. The genesis of the newly discovered giant wuben magmatic fe–ti oxide deposit in the emeishan large igneous province: A product of the late-stage redistribution and sorting of crystal slurries. *Mineralium Deposita* 54: 31–46.

Bédard, J.H. 2010. Parameterization of the Fe=Mg exchange coefficient (kd) between clinopyroxene and silicate melts. *Chemical Geology* 274: 169–176.

Berndt, J. 2004. An Experimental Investigation of the Influence of Water and Oxygen Fugacity on Differentiation of MORB at 200 MPa. *Journal of Petrology* 46: 135–167.

Breiman, L. 2001. Random Forests. *Machine Learning* 45: 5–32.

Breiman, L.; Friedman, J.; Olshen, R.A.; Stone, C.J. 2017. *Classification and regression trees*. Chapman and Hall/CRC, New York, 368p.

Brugger, C.R.; Hammer, J.E. 2010. Crystallization Kinetics in Continuous Decompression Experiments: Implications for Interpreting Natural Magma Ascent Processes. *Journal of Petrology* 51: 1941–1965.

Brzozowski, M.J.; Samson, I.M.; Gagnon, J.E.; Linnen, R.L.; Good, D.J. 2021. Effects of fluid-induced oxidation on the composition of Fe–Ti oxides in the eastern gabbro, coldwell complex, canada: implications for the application of Fe–Ti oxides to petrogenesis and mineral exploration. *Mineralium Deposita* 56: 601–618.

Buddington, A.F.; Lindsley, D.H. 1964. Iron-titanium oxide minerals and synthetic equivalents. *Journal of Petrology* 5: 311–357.

Canil, D. 1999. Vanadium partitioning between orthopyroxene, spinel and silicate melt and the redox states of mantle source regions for primary magmas. *Geochimica et Cosmochimica Acta* 63: 557–572.

Cao, Y.; Wang, C.Y.; Wei, B. 2020. Magma oxygen fugacity of mafic-ultramafic intrusions in convergent margin settings: insights for the role of magma oxidation states on magmatic Ni-Cu sulfide mineralization. *American Mineralogist* 105: 1841–1856.

Cawthorn, R.G. 2010. The Platinum Group Element Deposits of the Bushveld Complex in South Africa. *Platinum Metals Review* 54: 205–215.

Charlier, B.; Namur, O.; Latypov, R.; Tegner, C. 2015. *Layered intrusions*. In: Charlier, B.; Namur, O.; Latypov, R.; Tegner, C. (Eds.) *Springer Geology*. Springer Netherlands, Dordrecht, .

Chicchi, L.; Bindi, L.; Fanelli, D.; Tommasini, S. 2023. Frontiers of thermobarometry: GAIA, a novel deep learning-based tool for volcano plumbing systems. *Earth and Planetary Science Letters* 620: 118352.

Cortes, C.; Vapnik, V. 1995. Support-vector networks. *Machine Learning* 20: 273–297.

Davis, F.A.; Humayun, M.; Hirschmann, M.M.; Cooper, R.S. 2013. Experimentally determined mineral/melt partitioning of first-row transition elements (FRTE) during partial melting of peridotite at 3GPa. *Geochimica et Cosmochimica Acta* 104: 232–260.

Dygert, N.; Ji, D.; Etheridge, E.N. 2025. A predictive model for divalent element partitioning between clinopyroxene and basaltic melt and a europium-in-plagioclase-clinopyroxene oxybarometer for cumulate rocks. *Geochimica et Cosmochimica Acta* 394: 148–163.

Ganino, C.; Arndt, N.T.; Zhou, M.-F.; Gaillard, F.; Chauvel, C. 2008. Interaction of magma with sedimentary wall rock and magnetite ore genesis in the Panzhihua mafic intrusion, SW China. *Mineralium Deposita* 43: 677–694.

Ganino, C.; Arndt, N.T.; Chauvel, C.; Jean, A.; Athurion, C. 2013. Melting of carbonate wall rocks and formation of the heterogeneous aureole of the panzhihua intrusion, china. *Geoscience Frontiers* 4: 535–546.

Ge, R.-F.; Wilde, S.A.; Zhu, W.-B.; Wang, X.-L. 2023. Earth's early continental crust formed from wet and oxidizing arc magmas. *Nature* 623: 334–339.

Gennaro, E.; Paonita, A.; Iacono-Marziano, G.; Moussallam, Y.; Pichavant, M.; Peters, N.; et al. 2020. Sulphur Behaviour and Redox Conditions in Etnean Magmas during Magma Differentiation and Degassing. *Journal of Petrology* 61.

Ghiorso, M.S.; Evans, B.W. 2008. Thermodynamics of rhombohedral oxide solid solutions and a revision of the FE-TI two-oxide geothermometer and oxygen-barometer. *American Journal of Science* 308: 957–1039.

Grocolas, T.; Müntener, O.; Bloch, E.M.; Escrig, S.; Ulyanov, A.; Bouvier, A.-S. 2025. Cooling rates and melt extraction timescales determined by diffusion chronometry on shallow crustal plutonic rocks. *Contributions to Mineralogy and Petrology* 180: 45–66.

Hammond, P.A.; Taylor, L.A. 1982. The ilmenite/titano-magnetite assemblage: kinetics of re-equilibration. *Earth and Planetary Science Letters* 61: 143–150.

Hastie, T.; Tibshirani, R.; Friedman, J. 2009. *The elements of statistical learning*. In: *Springer Series in*

Statistics. Springer New York, New York, NY, .
Higgins, O.; Sheldrake, T.; Caricchi, L. 2022. Machine learning thermobarometry and chemometry using amphibole and clinopyroxene: A window into the roots of an arc volcano (mount liamuiga, saint kitts). *Contributions to Mineralogy and Petrology* 177: 10.
Hirschmann, M.M.; Withers, A.C.; Ardia, P.; Foley, N.T. 2012. Solubility of molecular hydrogen in silicate melts and consequences for volatile evolution of terrestrial planets. *Earth and Planetary Science Letters* 345–348: 38–48.
Holness, M.B.; Hallworth, M.A.; Woods, A.; Sides, R.E. 2007. Infiltration metasomatism of cumulates by intrusive magma replenishment: the wavy horizon, isle of rum, scotland. *Journal of Petrology* 48: 563–587.
Holycross, M.; Cottrell, E. 2022a. Experimental quantification of vanadium partitioning between eclogitic minerals (garnet, clinopyroxene, rutile) and silicate melt as a function of temperature and oxygen fugacity. *Contributions to Mineralogy and Petrology* 177: 21–43.
Holycross, M.; Cottrell, E. 2022b. Experimental quantification of vanadium partitioning between eclogitic minerals (garnet, clinopyroxene, rutile) and silicate melt as a function of temperature and oxygen fugacity. *Contributions to Mineralogy and Petrology* 177: 21.
Hou, T.; Botcharnikov, R.; Moulas, E.; Just, T.; Berndt, J.; Koepke, J.; et al. 2021. Kinetics of Fe–Ti oxide Re-equilibration in magmatic systems: implications for thermo-oxybarometry. *Journal of Petrology* 61: egaa116.
Lattard, D.; Sauerzapf, U.; Kontny, A. 2012. Rapid surficial oxidation of synthetic Fe-Ti oxides at high temperature: observations and consequences for magnetic measurements. *Geochemistry, Geophysics, Geosystems* 13: 2012GC004152.
Leuthold, J.; Blundy, J.; Ulmer, P. 2023. Trace element partitioning in basaltic systems as a function of oxygen fugacity. *Contributions to Mineralogy and Petrology* 178: 95.
Leuthold, J.; Blundy, J.D.; Holness, M.B.; Sides, R. 2014. Successive episodes of reactive liquid flow through a layered intrusion (unit 9, rum eastern layered intrusion, scotland). *Contributions to Mineralogy and Petrology* 168: 1021.
Li, Y. 2018. Temperature and pressure effects on the partitioning of V and Sc between clinopyroxene and silicate melt: implications for mantle oxygen fugacity. *American Mineralogist* 103: 819–823.
Liao, M.; Tao, Y.; Song, X.; Li, Y.; Xiong, F. 2016. Study of oxygen fugacity during magma evolution and ore genesis in the hongge mafic–ultramafic intrusion, the panxi region, SW china. *Acta Geochimica* 35: 25–42.
Loucks, R.R.; Fiorentini, M.L.; Rohrlach, B.D. 2018. Divergent T–$fO2$ paths during crystallisation of H2O-rich and H2O-poor magmas as recorded by Ce and U in zircon, with implications for TitaniQ and TitaniZ geothermometry. *Contributions to Mineralogy and Petrology* 173: 104–124.
Lundberg, S.; Lee, S.-I. 2017. A unified approach to interpreting model predictions. .
Lundberg, S.M.; Erion, G.; Chen, H.; DeGrave, A.; Prutkin, J.M.; Nair, B.; et al. 2020. From local explanations to global understanding with explainable AI for trees. *Nature Machine Intelligence* 2: 56–67.
Mallmann, G.; O'Neill, H.S.C. 2009. The Crystal/Melt Partitioning of V during Mantle Melting as a Function of Oxygen Fugacity Compared with some other Elements (Al, P, Ca, Sc, Ti, Cr, Fe, Ga, Y, Zr and Nb). 50.
Mallmann, G.; O'Neill, H.S.C. 2013. Calibration of an Empirical Thermometer and Oxybarometer based on the Partitioning of Sc, Yand V between Olivine and Silicate Melt. 54.
Namur, O.; Humphreys, M.C.S.; Holness, M.B. 2013. Lateral reactive infiltration in a vertical gabbroic

crystal mush, skaergaard intrusion, east Greenland. *Journal of Petrology* 54: 985–1016.
Namur, O.; Charlier, B.; Holtz, F.; Cartier, C.; McCammon, C. 2016. Sulfur solubility in reduced mafic silicate melts: Implications for the speciation and distribution of sulfur on Mercury. *Earth and Planetary Science Letters* 448: 102–114.
Okoye, K.; Hosseini, S. 2024. *R Programming: Statistical Data Analysis in Research*. Springer Nature Singapore, Singapore, .
Papike, J.J. 2005. Comparative planetary mineralogy: valence state partitioning of Cr, Fe, Ti, and V among crystallographic sites in olivine, pyroxene, and spinel from planetary basalts. *American Mineralogist* 90: 277–290.
Papike, J.J.; Burger, P.V.; Bell, A.S.; Le, L.; Shearer, C.K.; Sutton, S.R.; et al. 2013. Developing vanadium valence state oxybarometers (spinel-melt, olivine-melt, spinel-olivine) and V/(Cr+Al) partitioning (spinel-melt) for martian olivine-phyric basalts. *American Mineralogist* 98: 2193–2196.
Prokhorenkova, L.; Gusev, G.; Vorobev, A.; Dorogush, A.V.; Gulin, A. 2019. CatBoost: unbiased boosting with categorical features. .
Shepherd, K.; Namur, O.; Toplis, M.J.; Devidal, J.-L.; Charlier, B. 2022a. Trace element partitioning between clinopyroxene, magnetite, ilmenite and ferrobasaltic to dacitic magmas: an experimental study on the role of oxygen fugacity and melt composition. *Contributions to Mineralogy and Petrology* 177: 90.
Shepherd, K.; Namur, O.; Toplis, M.J.; Devidal, J.-L.; Charlier, B. 2022b. Trace element partitioning between clinopyroxene, magnetite, ilmenite and ferrobasaltic to dacitic magmas: an experimental study on the role of oxygen fugacity and melt composition. *Contributions to Mineralogy and Petrology* 177: 91–110.
Sievwright, R.H.; O'Neill, H.St.C.; Tolley, J.; Wilkinson, J.J.; Berry, A.J. 2020. Diffusion and partition coefficients of minor and trace elements in magnetite as a function of oxygen fugacity at 1150 °C. *Contributions to Mineralogy and Petrology* 175: 40.
Sossi, P.A.; Prytulak, J.; O'Neill, H.St.C. 2018. Experimental calibration of vanadium partitioning and stable isotope fractionation between hydrous granitic melt and magnetite at 800 °C and 0.5 GPa. *Contributions to Mineralogy and Petrology* 173: 27.
Tavazzani, L.; Peres, S.; Sinigoi, S.; Demarchi, G.; Economos, R.C.; Quick, J.E. 2020. Timescales and mechanisms of crystal-mush rejuvenation and melt extraction recorded in permian plutonic and volcanic rocks of the sesia magmatic system (southern alps, italy). *Journal of Petrology* 61: egaa049.
Toplis, M.J.; Carroll, M.R. 1995. An experimental study of the influence of oxygen fugacity on Fe-Ti oxide stability, phase relations, and mineral--melt equilibria in ferro-basaltic systems. *Journal of Petrology* 36: 1137–1170.
Toplis, M.J.; Corgne, A. 2002. An experimental study of element partitioning between magnetite, clinopyroxene and iron-bearing silicate liquids with particular emphasis on vanadium. *Contributions to Mineralogy and Petrology* 144: 22–37.
Van Orman, J.A.; Crispin, K.L. 2010. Diffusion in oxides. *Reviews in Mineralogy and Geochemistry* 72: 757–825.
Wang, G.-S.; Bai, Z.-J.; Hu, W.-J.; Gao, J.-F.; Zhu, W.-G.; Bai, Y.-X. 2025a. A machine learning-based V-in-olivine oxybarometer for characterizing oxygen fugacity in lunar and terrestrial basalts. *Earth and Planetary Science Letters* 671: 119692.
Wang J.; Xiong X.; Takahashi E.; Zhang L.; Li L.; Liu X. 2019. Oxidation State of Arc Mantle Revealed by Partitioning of V, Sc, and Ti Between Mantle Minerals and Basaltic Melts. *Journal of*

Geophysical Research: Solid Earth 124: 4617–4638.

Wang, K.; He, H.; Shi, W. 2025b. Geochemistry and mineralogy of ilmenite exsolutions in titanomagnetite and their implications for the ore-forming process at the damiao deposit. *Acta Geochimica* 44: 962–978.

Wei, Y.; Niu, Y.; Gong, H.; Duan, M.; Chen, S.; Guo, P.; et al. 2020. Geochemistry and iron isotope systematics of coexisting Fe-bearing minerals in magmatic Fe Ti deposits: a case study of the damiao titanomagnetite ore deposit, north China craton. *Gondwana Research* 81: 240–251.

Zeh, A.; Ovtcharova, M.; Wilson, A.H.; Schaltegger, U. 2015. The bushveld complex was emplaced and cooled in less than one million years – results of zirconology, and geotectonic implications. *Earth and Planetary Science Letters* 418: 103–114.

Zou, S.; Brzozowski, M.J.; Chen, X.; Xu, D. 2024. Machine-learning oxybarometer developed using zircon trace-element chemistry and its applications. *American Mineralogist* 109: 1181–1192.

Table 1. Modelling results and performance metrics for different oxybarometer algorithms

Values are reported as mean ± standard deviation. Algorithms are ordered within each oxybarometer by descending mean test R^2.

Model	Algorithm	Train R^2	Test R^2	Train RMSE	Test RMSE
Cpx–melt V partitioning model	CatBoost	0.993 ± 0.004	0.897 ± 0.044	0.050 ± 0.016	0.201 ± 0.032
	Random forest	0.985 ± 0.002	0.883 ± 0.047	0.079 ± 0.004	0.214 ± 0.033
	SVR	0.969 ± 0.015	0.880 ± 0.060	0.112 ± 0.029	0.216 ± 0.040
	Decision tree	0.962 ± 0.028	0.781 ± 0.091	0.115 ± 0.054	0.293 ± 0.047
V-in-Cpx-Mt oxybarometer	CatBoost	0.994 ± 0.004	0.828 ± 0.068	0.116 ± 0.038	0.616 ± 0.129
	Random forest	0.972 ± 0.008	0.794 ± 0.073	0.256 ± 0.033	0.677 ± 0.133
	SVR	0.975 ± 0.012	0.775 ± 0.074	0.234 ± 0.073	0.712 ± 0.136
	Decision tree	0.935 ± 0.035	0.612 ± 0.136	0.375 ± 0.121	0.927 ± 0.150
Mt–melt V partitioning model	CatBoost	0.998 ± 0.002	0.831 ± 0.071	0.032 ± 0.014	0.275 ± 0.070
	SVR	0.989 ± 0.019	0.804 ± 0.081	0.053 ± 0.053	0.295 ± 0.073
	Random forest	0.972 ± 0.005	0.781 ± 0.089	0.119 ± 0.009	0.313 ± 0.076
	Decision tree	0.959 ± 0.037	0.599 ± 0.179	0.122 ± 0.075	0.418 ± 0.095
V-in-Mt oxybarometer	CatBoost	0.998 ± 0.002	0.836 ± 0.102	0.075 ± 0.031	0.661 ± 0.226
	SVR	0.977 ± 0.039	0.813 ± 0.175	0.216 ± 0.147	0.677 ± 0.322
	Random forest	0.966 ± 0.011	0.803 ± 0.113	0.319 ± 0.052	0.730 ± 0.233
	Decision tree	0.950 ± 0.041	0.646 ± 0.198	0.345 ± 0.173	0.966 ± 0.259

V-in-Cpx oxybarometer	Random forest	0.980 ± 0.004	0.865 ± 0.045	0.391 ± 0.038	0.981 ± 0.144
	CatBoost	0.931 ± 0.010	0.861 ± 0.037	0.732 ± 0.053	1.002 ± 0.126
	SVR	0.937 ± 0.030	0.782 ± 0.093	0.690 ± 0.146	1.241 ± 0.251
	Decision tree	0.955 ± 0.030	0.757 ± 0.084	0.555 ± 0.205	1.312 ± 0.199

Note: R^2 = coefficient of determination; RMSE = root mean square error.

Figure captions

Fig. 1. Compositional distribution of the three experimental datasets in melt, magnetite, and clinopyroxene compositional spaces. (a) Total alkali–silica (TAS) diagram for melt compositions, showing SiO_2 versus $Na_2O + K_2O$. (b) $FeO–Fe_2O_3–TiO_2$ ternary diagram for magnetite compositions, with major oxide end-member fields indicated. (c) Wo–En–Fs ternary diagram for clinopyroxene compositions. Purple circles, coral squares, and cyan triangles represent the Cpx–Melt, Mt–Melt, and Cpx–Mt datasets, respectively.

Fig. 2. Predictive performance of the clinopyroxene and melt vanadium partitioning model and the V-in-clinopyroxene oxybarometer. (a) Predicted versus observed $\log D_V$ values for the clinopyroxene and melt partitioning model. (b) Predicted versus observed fO_2, expressed as ΔFMQ, for the V in clinopyroxene oxybarometer. Blue and orange symbols represent the training and test datasets, respectively. Red dashed lines indicate the 1:1 relationship, whereas black dashed lines show deviations of ±0.2 log units in panel (a) and ±0.5 ΔFMQ in panel (b). Model performance is summarized by the reported R^2 and root mean square error values.

Fig.3. Predictive performance of the magnetite and melt vanadium partitioning model and the V in magnetite oxybarometer. (a) Comparison between predicted and observed $\log D_V$ values for vanadium partitioning between magnetite and melt. (b) Comparison between

924 predicted and observed fO_2 (ΔFMQ) values obtained using the V in magnetite oxybarometer.
925 Blue and red symbols represent the training and test datasets, respectively. Red dashed lines
926 indicate the 1:1 relationship, and black dashed lines delimit deviations of ± 0.2log units in
927 panel (a) and ±0.5 ΔFMQ in panel (b). The corresponding $R^2$and root mean square error values
928 are shown in each panel.

929 **Fig.4. Predictive performance of the V in clinopyroxene and magnetite oxybarometer.**
930 Predicted ΔFMQ values are plotted against the corresponding observed values for the training
931 and test datasets. Purple and pink symbols represent training and test data, respectively. The
932 red dashed line indicates the 1:1 relationship, whereas the black dashed lines define deviations
933 of ±0.5 ΔFMQ. The model yields R^2= 0.979 and a root mean square error of 0.225 ΔFMQ

934 **Fig.5 Feature importance and SHAP analysis of the top ten variables in the clinopyroxene**
935 **and melt models.** (a) Relative feature importance and SHAP distributions for the prediction of
936 vanadium partitioning between clinopyroxene and melt. (b) Corresponding results for the V in
937 clinopyroxene oxybarometer. Horizontal bars show the normalized contribution of each input
938 variable to model prediction, whereas the SHAP distributions illustrate the magnitude and
939 direction of its effect. Symbol color represents the original feature value, ranging from low
940 values in blue to high values in pink. fO_2 is the dominant control on the predicted partition
941 coefficient, whereas $D_V$is the principal control on fO_2 calculated using the V in clinopyroxene
942 oxybaromete

943 **Fig.6. Feature importance and SHAP analysis of the top ten variables in the magnetite**
944 **and melt models.** (a) Relative importance and SHAP distributions of variables controlling
945 vanadium partitioning between magnetite and melt. (b) Corresponding results for the V in
946 magnetite oxybarometer. Bars show the normalized contribution of each feature, and SHAP

values indicate whether individual observations increase or decrease the predicted response. Colors represent feature magnitude from low values in blue to high values in pink. fO_2 and magnetite TiO_2 are the principal controls on the partitioning model, whereas D_V, melt TiO_2 and magnetite composition exert the strongest influence on the oxybarometer.

Fig.7 Feature importance and SHAP analysis of the top ten variables in the V in clinopyroxene and magnetite oxybarometer. The bar plot shows the normalized importance of the ten most influential model variables, and the accompanying SHAP distributions show the direction and magnitude of their contributions to predicted fO_2 (ΔFMQ). Colors represent feature values from low in blue to high in pink. The vanadium partition coefficient provides the largest contribution to model predictions, followed by magnetite FeO and clinopyroxene Al_2O_3 with additional contributions from the major element compositions of both minerals.

Fig.8. Evaluation of the V in clinopyroxene and magnetite oxybarometer using paired mineral data(Shepherd et al. 2022*a*)**.** (a) Comparison between observed and predicted magnetite to clinopyroxene vanadium partition coefficients. Open circles represent individual samples connected by dashed lines, whereas diamonds and error bars summarize the mean and standard deviation of the observed and predicted datasets. (b) Comparison between predicted and independently constrained fO_2 (ΔFMQ) values. The dark dashed line indicates the 1:1 relationship, and the lighter lines represent deviations of ±0.5 ΔFMQ error bars show the uncertainties associated with individual estimates.

Fig.9 Validation of V partitioning oxybarometers using natural samples. (a) Comparison of fO_2 (ΔFMQ) values calculated using the V in clinopyroxene and V in olivine oxybarometers for samples from Dali and Lijiang. (b) Comparison of results from the Eu in clinopyroxene and plagioclase and V in clinopyroxene and magnetite oxybarometers for samples 206R 3 W and

238R 2 W. In panels (a) and (b), the dark dashed line represents the 1:1 relationship, lighter lines indicate deviations of ±0.5 ΔFMQ, and error bars show the associated uncertainties. (c) Distributions of ΔFMQ estimates for the Panzhihua intrusion obtained using the V in magnetite, V in clinopyroxene and magnetite, and V in clinopyroxene oxybarometers. Violin envelopes show data density, individual symbols represent calculated values, and the internal boxes summarize the central distribution.

Fig. 10. Stratigraphic variations in fO_2, Fe and Ti oxide abundance, and clinopyroxene Mg number in the Panzhihua and Bushveld layered intrusions. (a) Variation in fO_2 (ΔFMQ) with height above the basal contact in the Panzhihua intrusion. (b) Stratigraphic variation in the modal abundance of Fe and Ti oxides in Panzhihua. (c) Relationship between fO_2 and clinopyroxene Mg number for the Panzhihua samples. (d) Variation in fO_2 with borehole depth in the Bushveld Complex. (e) Variation in Fe and Ti oxide abundance with borehole depth in Bushveld. (f) Relationship between fO_2 and clinopyroxene Mg number for the Bushveld samples. Dashed lines in panels (c) and (f) show linear regressions, shaded regions represent their confidence intervals, and the corresponding R^2 values are reported in each panel.